THERMOMAGNETIC REACTIVE ETHYLENE GLYCOL-METALLIC NANOFLUID TRANSPORT FROM A CONVECTIVELY HEATED POROUS SURFACE WITH OHMIC DISSIPATION, HEAT SOURCE, THERMOPHORESIS AND BROWNIAN MOTION EFFECTS

MD. Shamshuddin[1*],

[1]*Department of Mathematics, Vaagdevi College of Engineering (Autonomous), Bollikunta, Warangal-506005, Telangana State, **India**.*
Email: shamshuddin_md@vaagdevi.edu.in

Fazle Mabood[2],

[2]*Department of Information Technology, Fanshawe College London, Ontario, **Canada**.*
Email: mabood1971@yahoo.com

O. Anwar Bég[3]

[3] *Professor of Engineering Science & Director- Multi-Physical Engineering Sciences Group, Mechanical Engineering Department, School of Science, Engineering and Environment (SEE), University of Salford, Manchester, M54WT, **UK**.*
Email: O.A.Beg@salford.ac.uk /gortoab@gmail.com

*Corresponding author: email: shamshuddin_md@vaagdevi.edu.in (or) shammaths@gmail.com

Abstract

The objective of this study is to develop a mathematical model for chemically reacting magnetic nanofluid flow with thermophoretic diffusion, Brownian motion and Ohmic magnetic heating in a Darcian permeable regime. The current flow model also considers a number of different nanofluid types i.e. Cu, Ag and Au nanoparticles with base fluid ethylene glycol. Effectively a nanoscale formulation combining the Buongiorno two-component model with the Tiwari-Das model is deployed so that a nanoparticle species diffusion equation is also included as well as material properties for specific nanoparticles and base fluids. By means of similarity transformations, non-linear dimensionless ordinary differential equations are derived (from the original partial differential equations) and solved numerically by means of Runge-Kutta-Fehlberg-fourth fifth order method. The effect of emerging parameters on velocity, temperature, concentration, skin friction, Nusselt number and Sherwood number profiles is visualized graphically. Validation with earlier studies is included. The computations show that temperatures are suppressed with greater thermal Grashof and Biot numbers. Nanoparticle-concentrations are strongly diminished with increasing reactive species and Lewis number, whereas Sherwood number is elevated with stronger chemical reaction effect. The study is relevant to magnetic nanomaterials processing.

1. Introduction

Nanotechnology has emerged as a major focus in 21st century engineering. It involves the synthesis of materials engineered at the nanoscale which include graphene, nanowires, nanotubes etc. A sub-branch of these nanomaterials of great interest in thermofluid sciences is nanofluids. First introduced by Choi and Eastman [1] nanofluids are colloidal suspensions of nanoparticles in a base fluid e.g. water, oils etc. Generally, metal or metal oxides are used for nanofluids, although carbon materials can also be used. The attraction of nanofluids is the heat conductivity elevation while simultaneously avoiding agglomeration and clustering problems (associated with larger scale particles), thereby mitigating problems in engineering operations, as emphasized by Ogunseye *et al.* [2]. Magnetic nanofluids are a further subset of nanofluids and refer to liquids which respond to external magnetic fields resulting in magnetohydrodynamic (MHD) nanofluid flows. These flows are important in for example nanomaterials synthesis, manufacturing flows and coating dynamics wherein external magnetic fields can be deployed to produce specific characteristics of the nanofluids for different applications. Numerous researchers have therefore employed mathematical models and experimental techniques in *magnetic nanofluid dynamics* using for a variety of geometrical configurations. Makinde and Mishra [3] analyzed the radiative heat flux in magnetohydrodynamic (MHD) nanofluid boundary layer flow from an extending surface. Ramesh *et al.* [4] considered magnetohydrodynamic nanofluid flow with heat generation/absorption. Rajesh *et al.* [5] deployed a finite difference technique to compute the unsteady hydromagnetic dissipative nanofluid boundary layer flow from an impulsively started vertical surface with wall suction/injection effects. Prasad *et al.* [6] presented Keller box finite difference solutions for external coating flow of a magnetic nanofluid on a spherical body in porous media. Uddin *et al.* [7] presented one of the first numerical simulations of slip effects on magnetohydrodynamic nanofluid stretching/shrinking sheet materials processing using MAPLE quadrature. They observed considerable modification in momentum, thermal and nanoparticle species diffusion characteristics with increasing magnetic field effects. Anwar Bég *et al.* [8] studied thermocapillary effects on hydromagnetic nanofluid convection in bio-nanocoating flows with electromagnetic induction at generalized magnetic Prandtl numbers. Rarani *et al.* [9] studied experimentally the influence of alternating and direct electrical fields on viscosity of Fe_3O_4-EG - Ethylene glycol magnetic nanofluid). Further studies of magnetohydrodynamic nanofluid transport have been communicated by Kandasamy *et al.* [10] (who considered wall transpiration effects) and Anwar Bég *et al.* [11] (on titanium dioxide/aluminium oxide-water nanofluids with magnetic induction effects).

In many of the above studies Brownian and thermophoresis dynamics effects were also confirmed to have a significant influence on thermal characteristics of nanofluids. Thermophoresis is associated with the migration of particles under a thermal gradient. Brownian movement is generated by the persistent bombardment (ballistic collisions) of the molecules in fluids. Both effects are significant in nanofluid convective transport. Makinde and Animasaun [12] reported the impact of thermophoresis and Brownian motion on nanoliquid boundary layer flow with non-linear thermal radiation and quartic chemical reaction effects from a curved geometry. Mondal *et al.* [13] presented numerical solutions for unsteady viscoplastic nanofluid flow with Brownian motion and thermophoresis effects. Pakravan and Yaghoubi [14] considered the collective impact of Dufour diffusion-thermal gradient, thermophoresis and Brownian motion on nanofluid free convection. Kuznetsov and Nield [15] employed Buongiorno's nanoscale model to compute thermophoresis and Brownian motion effects on natural convection nanofluid boundary layer flow. Aminfar and Haghgoo [16] studied

alumina-water nanofluid boundary layer flow, noting that thermophoresis suppresses nanoparticle concentrations, and achieving good correlation with experimental studies.

The above studied generally neglected *chemical reaction effects* which frequently arise in industrial coating and materials fabrication. In many nanofluid processes, *chemical reactions* may also arise. Reactions are *homogeneous* when they materialize uniformly through a given phase, or *heterogeneous when they vary through a medium*. Both destructive and constructive reactions may occur. Chemical reaction is of order one if the reaction rate is directly proportional to the concentration of the original reacting species. Shamshuddin and Eid [17] investigated the effects of nth order reacting agents on hydromagnetic mixed convection nanofluid flow from an extending sheet. Zhang *et al.* [18] explored the variable surface heat flux impact on chemically reactive nanofluid flow utilizing the Differential Transform method (DTM). Qayyum *et al.* [19] employed a homogenous-heterogenous reaction model to compute the heat transfer in Ag-water and Cu-water nanofluid external boundary layer flow from a stretching cylinder with Euler's explicit method. In these investigations, chemical reaction was formulated by considering destructive/generative type of reactive species which arises, as noted earlier, in materials synthesis and coating operations. Various reactive fluid dynamics materials processing models relevant to such applications have been presented by Salawu *et al.* [20] (double exothermic reactions), Shamshuddin *et al.* [21] (magnetic non-Newtonian coating flow with homogenous-heterogenous reactions) Aleem *et al.* [22] ($TiO_2/Al_2O_3/CuO$-water based nanofluids in chemically reactive flows in porous media) and Ullah et al. [23] (time-dependent coating wedge flows of viscoplastic magnetic nanofluids with generative/destructive chemical reaction).

To the knowledge of the authors', based on scrutiny of the literature, *heat transport in nanofluid external boundary layer from a heated stretching vertical wall to a porous medium (Darcian regime saturated with the nanofluid), with a range of metallic nanoparticles (copper, silver, gold), convective heating and chemical reaction in ethylene glycol base fluid*, has thus far *not been considered in the scientific literature. This is the focus of the present article*. Additionally, *viscous heating, Ohmic magnetic heating (Joule dissipation) and heat generation effects* are included in the mathematical model. Thermophoresis and Brownian motion effects featured in the Buongiorno nanoscale model are also combined with nanoparticle volume fraction features from the Tiwari-Das model. *The novelty of the current study is therefore the simultaneous consideration of all these multiple nanoscale, hydrodynamic, electromagnetic, chemical and thermophysical effects which have previously been considered separately*. An efficient MATLAB-based numerical quadrature technique known as the RKFM-45 method is utilized to obtain solutions to the dimensionless, transformed boundary layer equations subject to carefully prescribed wall and free stream boundary conditions. Validation with previous studies is included. The simulations are useful in assessing the transport characteristics of magnetic nano-coating of industrial components and furnishing a deeper insight into simultaneous influence of many different phenomena which arise in magnetic-nanofluid materials processing.

2. Mathematical magnetic nanofluid transport model

Steady, incompressible, two-dimensional, laminar, magnetohydrodynamic flow of a nanofluid with Ohmic dissipation, thermophoresis and Brownian motion along a linearly stretching porous vertical plate adjacent to a porous medium (Darcian) is considered. Additionally, the energy and concentration equations are modified with the inclusion of heat source and destructive reacting agents. The flow is restrained to $y \geq 0$, which displayed in

Fig. 1. The stretching velocity along $x-$ axis is $u = u_w(x) = ax$, with moving plate $a > 0$. C is concentration and T is temperature of the nanofluid. While surface and ambient concentration are C_f, C_∞ and convective surface and ambient temperature are T_f, T_∞ respectively. A uniform static magnetic field acts transverse to the vertical surface. Magnetic induction is neglected. In view of the above approximations, the governing boundary layer approximation equations for magnetic nanofluid flow are extended from [24-25] to consider multiple nanoparticle effects and heat generation in addition to viscous dissipation and Ohmic (Joule) magnetic dissipation effects:

$$\frac{\partial u}{\partial u} + \frac{\partial v}{\partial y} = 0,$$

(1)

$$u\frac{\partial u}{\partial x} + v\frac{\partial u}{\partial y} = \frac{\mu_{nf}}{\rho_{nf}}\frac{\partial^2 u}{\partial y^2} + g\beta_{nf}\left(T - T_\infty\right) - \left(\frac{\sigma_{nf}B_0^2}{\rho_{nf}} + \frac{\nu_{nf}}{k_p^*}\right)u,$$

(2)

$$u\frac{\partial T}{\partial x} + v\frac{\partial T}{\partial y} = \frac{k_{nf}}{(\rho c_p)_{nf}}\frac{\partial^2 T}{\partial y^2} + \frac{\mu_{nf}}{(\rho c_p)_{nf}}\left(\frac{\partial u}{\partial y}\right)^2 + \frac{\sigma_{nf}B_0^2}{(\rho c_p)_{nf}}u^2 + \tau\left\{D_B\frac{\partial T}{\partial y}\frac{\partial C}{\partial y} + \frac{D_T}{T_\infty}\left(\frac{\partial T}{\partial y}\right)^2\right\}$$

$$+ \frac{Q^*}{(\rho c_p)_{nf}}\left(T - T_\infty\right),$$

(3)

$$u\frac{\partial C}{\partial x} + v\frac{\partial C}{\partial y} = D_B\frac{\partial^2 C}{\partial y^2} + \frac{D_T}{T_\infty}\frac{\partial^2 T}{\partial y^2} - K_r'\left(C - C_\infty\right)$$

(4)
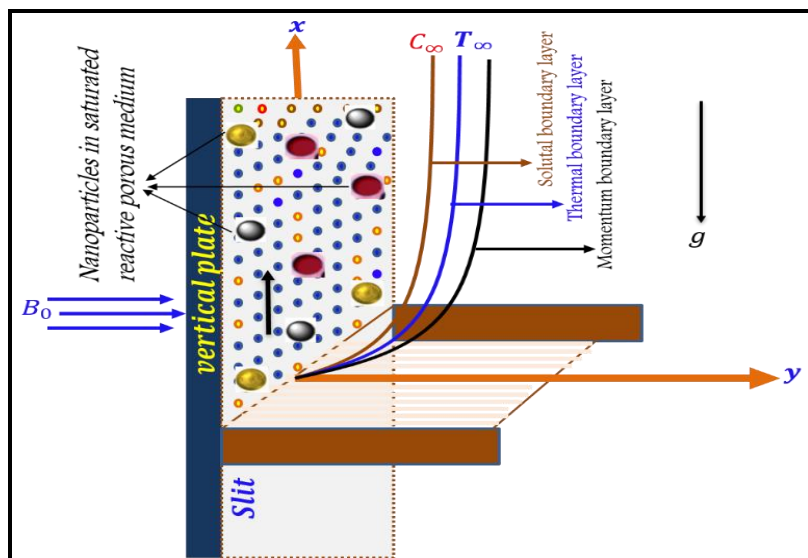
Fig. 1. Physical model for heated vertical plate

The relevant boundary conditions at the wall and in the free stream are:

$$u = U_0 = ax, \quad v = 0, \quad -k_{nf}\frac{\partial T}{\partial y} = h_f\left(T_f - T\right), \quad D_B\frac{\partial C}{\partial y} + \frac{D_T}{T_\infty}\frac{\partial T}{\partial y} \quad at \; y = 0$$

$$u \to 0, \quad T \to T_\infty, \quad C \to C_\infty \quad\quad\quad as \; y \to \infty$$

(5)

Following [11], nanofluid properties are computed using the following relations:

$$\rho_{nf} = (1-\varphi)\rho_f + \varphi\rho_s, \quad \mu_{nf} = \frac{\mu_f}{(1-\varphi)^{\frac{5}{2}}},$$

$$(\rho c_p)_{nf} = (1-\varphi)(\rho c_p)_f + \varphi(\rho c_p)_s, \tag{6}$$

$$k_{nf} = k_f \left[\frac{k_s + 2k_f - 2\varphi(k_f - k_s)}{k_s + 2k_f + 2\varphi(k_f - k_s)} \right]$$

Following [26], σ_{nf} i.e., effective electrical conductivity of nanofluid is considered as follows:

$$\sigma_{nf} = \sigma_f \left[1 + \frac{3(r-1)\varphi}{\{(r+2)-(r-1)\varphi\}} \right], \qquad r = \frac{\sigma_s}{\sigma_f} \tag{7}$$

Table 1: Following [27] and [25], thermo-physical properties of nanoparticles with base fluid

Thermo-physical properties	Base fluid	Nanoparticles		
	$C_2H_6O_2$ (Ethylene-Glycol)	Cu (Copper)	Ag (Silver)	Au (Gold)
ρ (Kgm^{-3})	1115	8933	10500	19300
c_p $(JKg^{-1}K^{-1})$	2430	385	235	129.1
k $(Wm^{-1}K^{-1})$	0.253	401	429	318
$\beta \times 10^{-5}$ (K^{-1})	5.7	1.67	1.89	1.4
σ (Sm^{-1})	10.7x10^{-5}	5.96x10^7	6.30x10^7	4.25x10^7

The following similarity transformations are implemented:

$$\left. \begin{array}{l} \eta = y\left(a/v_f\right)^{1/2}, \psi(x,y) = \left(av_f\right)^{1/2} x f(\eta), T = T_\infty + \left(T_f - T_\infty\right)\theta(\eta), \\[2mm] C = C_\infty + \left(C_f - C_\infty\right)\phi(\eta), u = \frac{\partial\psi}{\partial y} = a x f'(\eta), \quad v = -\frac{\partial\psi}{\partial x} = -\left(av_f\right)^{1/2} f(\eta), \end{array} \right\}, \tag{8}$$

Clearly equation (1) is satisfied automatically and inserting Eqn. (8) into Eqns. (2) – (7) yields:

Momentum

$$f''' + A_1 A_2 \left(f f'' - f'^2 \right) + A_1 A_2 A_3 Gr \theta - M A_1 A_4 f' - \left(1/K_p\right) f' = 0 \tag{9}$$

Energy

$$\frac{A_5}{Pr} \theta'' + \frac{1}{A_1} Ec \left(f'' \right)^2 + A_4 M Ec \left(f' \right)^2 + A_6 f \theta' + Nb \theta' \phi' + Nt \theta'^2 + Q \theta = 0 \tag{10}$$

Nanoparticle Species

$$\frac{1}{Le} \phi'' + \frac{1}{Le} \frac{Nt}{Nb} \theta'' + f \phi' - Kr \phi = 0 \tag{11}$$

With boundary conditions

$$\left. \begin{array}{l} f = 0, \quad f' = 1, \quad \theta' = -Bi(1-\theta), \quad Nb\theta'(0) + Nt\phi'(0) = 0 \quad at \ \eta = 0 \\[2mm] f' \to 0, \ h \to 0, \ \theta \to 0, \quad \phi \to 0 \qquad when \ \eta \to \infty \end{array} \right\} \tag{12}$$

$A_1, A_2, A_3, A_4, A_5, A_6$ as arising in the above equations are functions for volume fraction and thermophysical properties, defined as:

$$A_1 = (1-\varphi)^{\frac{5}{2}}, \quad A_2 = \left(1 - \varphi + \varphi \frac{\rho_s}{\rho_f}\right), \qquad A_3 = \left(1 - \varphi + \varphi \frac{\beta_s}{\beta_f}\right),$$

$$A_4 = \left\{1 + \frac{3(r-1)\varphi}{\{(r+2)-(r-1)\varphi\}}\right\}, \quad A_5 = \frac{k_{nf}}{k_f}, \quad A_6 = \left(1 - \varphi + \varphi \frac{(\rho c_p)_s}{(\rho c_p)_f}\right) \tag{13}$$

Also

$$
\left.
\begin{aligned}
&Gr = \frac{g\beta_f\left(T_f - T_\infty\right)}{a\,U_0}, M = \frac{\sigma_f B_0^2}{a\,\rho_f}, K_p = \frac{k_p^*}{v_f}, \mathrm{Pr} = \frac{v_f(\rho c_p)_f}{k_f}, Q = \frac{Q^*}{a(\rho c_p)_f}, \\
&Ec = \frac{U_0^2}{(c_p)_f\left(T_f - T_\infty\right)}, Nt = \frac{(\rho c_p)_s D_T\left(T_f - T_\infty\right)}{(\rho c_p)_f T_\infty v_f}, Nb = \frac{(\rho c_p)_s D_B\left(C_f - C_\infty\right)}{(\rho c_p)_f v_f}, \\
&Le = \frac{v_f}{D_B}, Kr = \frac{K_r^*}{a}, Bi = \frac{h_f}{k_{nf}}\sqrt{\frac{v_f}{a}}
\end{aligned}
\right\}, \tag{14}
$$

The *dimensionless* shear stress i.e. skin friction, heat transfer rate (local Nusselt number) and nanoparticle mass transfer rate (local Sherwood number) at the plate surface are important in materials processing design and may be mathematically stated as follows:

$$C_f = \frac{2\tau_w}{\rho_f U_0^2}\bigg|_{y=0}, \quad Nu_x = \frac{x\,q_w}{k_f\left(T_f - T_\infty\right)}, \quad Sh_x = \frac{x\,J_w}{D_B\left(C_f - C_\infty\right)} \tag{15}$$

Here τ_w, q_w, J_w are shear stress, heat and mass fluxes respectively. They are expressed as,

$$\tau_w = -\mu_{nf}\left(\frac{\partial u}{\partial y}\right)\bigg|_{y=0}, q_w = -k_{nf}\left(\frac{\partial T}{\partial y}\right)\bigg|_{y=0}, J_w = -D_B\left(\frac{\partial C}{\partial y}\right)\bigg|_{y=0} \tag{16}$$

In dimensionless form C_f, Nu and Sh can be expressed as:

$$\sqrt{\mathrm{Re}_x}\,(1-\phi)^{\frac{5}{2}}\,C_f = -2f''(0), \quad A_5\frac{Nu_x}{\sqrt{\mathrm{Re}_x}} = -\theta'(0), \quad \frac{Sh_x}{\sqrt{\mathrm{Re}_x}} = -\phi'(0) \tag{17}$$

$\mathrm{Re}_x = xU_0/v_f$ signifies local Reynolds number based on location along the vertical plate (x).

3. Numerical procedure and validation

3.1 Numerical technique

Closed-form solutions of the transformed boundary layer Eqns. (9)-(11) with related boundary conditions (12) are intractable since the equations are strongly non-linear and coupled in nature. Nonetheless, robust solutions can be computed numerically utilizing stable, efficient Runge–Kutta Fehlberg (RKF-45) quadrature in MATLAB symbolic software with a shooting technique that can accommodate complex boundary conditions and multiple nonlinear coupled terms (mixed derivatives). The RK45 algorithm is based on a *collocation method* in which a finite-dimensional space of candidate solutions is selected (usually, polynomials up to a certain degree) and a number of points in the domain (called *collocation points*), and a solution selected which satisfies the given equation at the collocation points. The stepping formulae in RK45 are summarized below [11]:

$$k_0 = f\left(x_i, y_i\right), \tag{18}$$

$$k_1 = f\left(x_i + \frac{1}{4}h, y_i + \frac{1}{4}hk_0\right), \tag{19}$$

$$k_2 = f\left(x_i + \frac{3}{8}h, y_i + \left(\frac{3}{32}k_0 + \frac{9}{32}k_1\right)h\right), \tag{20}$$

$$k_3 = f\left(x_i + \frac{12}{13}h, y_i + \left(\frac{1932}{2197}k_0 - \frac{7200}{2197}k_1 + \frac{7296}{2197}k_2\right)h\right), \tag{21}$$

$$k_4 = f\left(x_i + h, y_i + \left(\frac{439}{216}k_0 - 8k_1 + \frac{3860}{513}k_2 - \frac{845}{4104}k_3\right)h\right), \tag{22}$$

$$k_5 = f\left(x_i + \frac{1}{2}h, y_i + \left(-\frac{8}{27}k_0 + 2k_1 - \frac{3544}{2565}k_2 + \frac{1859}{4101}k_3 - \frac{11}{40}k_4\right)h\right), \tag{23}$$

$$y_{i+1} = y_i + \left(\frac{25}{216}k_0 + \frac{1408}{2565}k_2 + \frac{2197}{4101}k_3 - \frac{1}{5}k_4\right)h, \tag{24}$$

$$z_{i+1} = z_i + \left(\frac{16}{135}k_0 + \frac{6656}{12825}k_2 + \frac{28561}{56430}k_3 - \frac{9}{50}k_4 + \frac{2}{55}k_5\right)h. \tag{25}$$

Here y denotes fourth order Runge-Kutta phase and z is the fifth order Runge-Kutta phase. An estimate of the error is achieved by subtracting the two values obtained. If the error exceeds a specified threshold, the results can be re-calculated using a smaller step size. The approach to estimating the new step size is shown below:

$$h_{new} = h_{old}\left(\frac{\varepsilon h_{old}}{2|z_{i+1} - y_{i+1}|}\right)^{1/4}. \tag{26}$$

The appropriate variable e.g. velocity, temperature, nanoparticle concentration is computed in a sub-iteration loop. The robustness and stability of this numerical method is therefore well established- it is highly adaptive since it adjusts the quantity and location of grid points during iteration and thereby constrains the local error within acceptable specified bounds. Many different wall boundary conditions are easily accommodated."

The impact of the emerging nanoscale, thermophysical and hydrodynamic parameters on the non-dimensional velocity, temperature, nanoparticle concentration, skin friction, Nusselt and Sherwood numbers has been computed. The step size of $\Delta\eta = 0.01$ with a precision reaching up to the fifth decimal point, is prescribed as the convergence criterion. In all figures, we prescribe the data values (unless otherwise declared) as $M = 0.5, Q = 0.2, \phi = Nb = Nt = 0.1, \ \mathrm{K}_P = 100, Bi = Gr = Ec = 1, Kr = Le = 1, \mathrm{Pr} = 6.2$. These correspond to physically viable scenarios with weak magnetic field, high permeability porous media, strong viscous heating and metallic-doped ethylene glycol nanofluid and are based on previous studies which utilize industrially realistic data [5]-[8]:

3.2. *Verification of numerical code*

To authenticate the validity of the MATLAB numerical solutions, velocity gradient, and temperature gradient for limiting values of M, Nb and Nt are compared with Mabood and Das [28], Xu and Li [29], Khan and Pop [30], and Mabood *et al.* [31] as recorded in **Tables 2-3**. Excellent agreement is achieved with the earlier computations obtained by Mabood and Das [28] and Xu and Lee [29] for *forced convection of viscous fluids in the absence of nanoparticles* (Table 2) and Khan and Pop [30] and Mabood *et al.* [31] for forced convection,

non-dissipative flow in the absence of heat source/sink, chemical reaction and no convective heating at the wall (Table 3): Confidence in the present MATLAB solutions is therefore justifiably high.

Table 2. Comparison of current results with literature for $-f''(0)$ with variation of M when $\varphi = Gr = 0, K_p \to \infty$.

M	Mabood and Das [28]	Xu and Lee [29]	Present results
0.0	1.000008	-	1.00000
1.0	1.4142135	1.41421	1.414214
5.0	2.4494897	2.4494	2.449489
10	3.3166247	3.3166	3.316624
50	7.1414284	7.1414	7.141429
100	10.049875	10.0498	10.04988
500	22.383029	22.38302	22.38303
1000	31.638584	-	31.63858

Table 3. Comparison of current results with literature for $-\theta'(0)$ with variation of Nb and Nt when $\varphi = Gr = Ec = Q = Kr = 0, \Pr = Le = 10, K_p = Bi \to \infty$.

$Nb = Nt$	Khan and Pop [30]	Mabood *et al.* [31]	Present results
0.1	0.9524	0.95237	0.952376
0.2	0.3654	0.36536	0.365358
0.3	0.1355	0.13551	0.135514
0.4	0.0495	0.04946	0.049465
0.5	0.0179	0.01792	0.017922

4. Numerical results and interpretation

A broad range of RKFM-45 computations have been performed and all graphical results for velocity, temperature, nanoparticle concentration, skin friction, Nusselt number and Sherwood number plot for key parameters in **Figs. 2-12**. Ethylene-glycol is considered as the base fluid with three different metallic nanoparticles (Cu, Ag and Au).
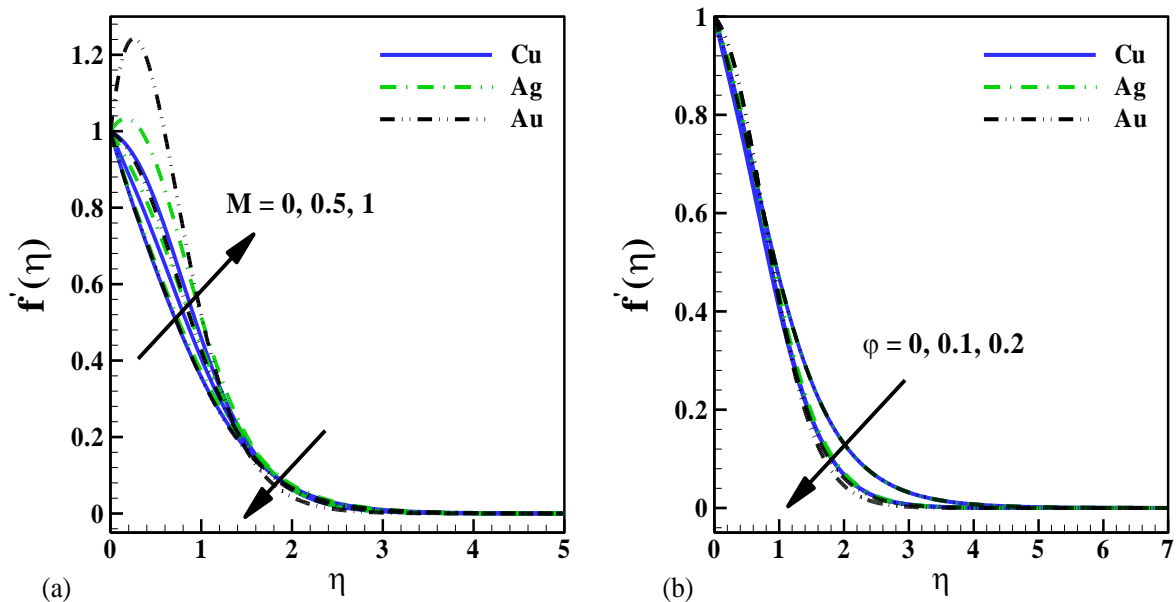
Fig. 2. Effects of magnetic parameter (M) and solid volume fraction (φ) on velocity.
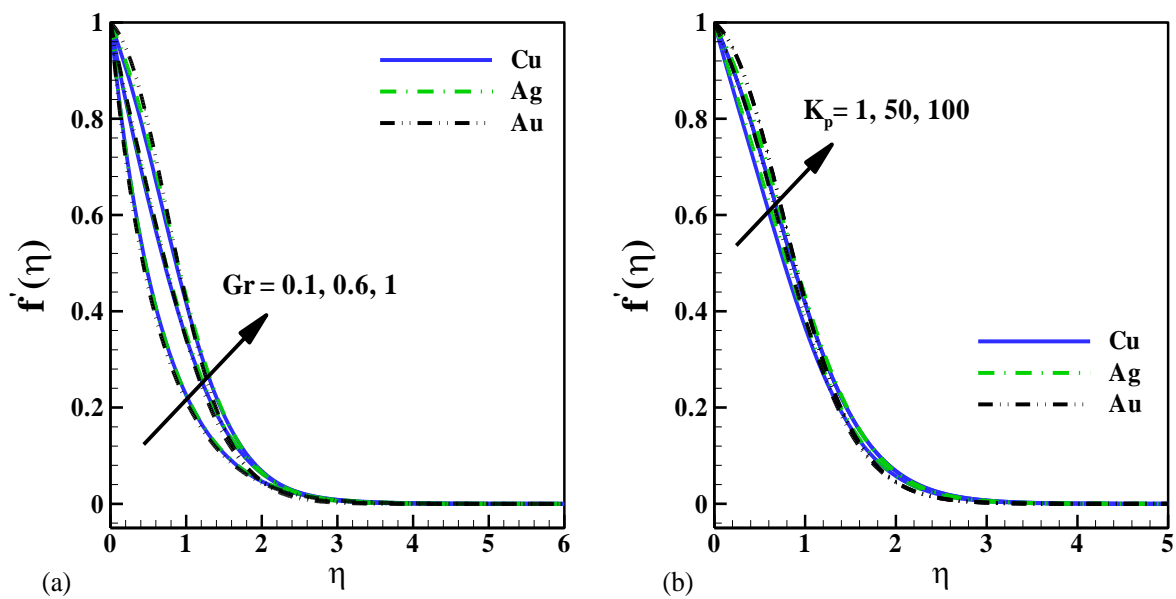
Fig. 3. Effects of thermal Grashof number (Gr) and permeability parameter (K_p) on velocity.
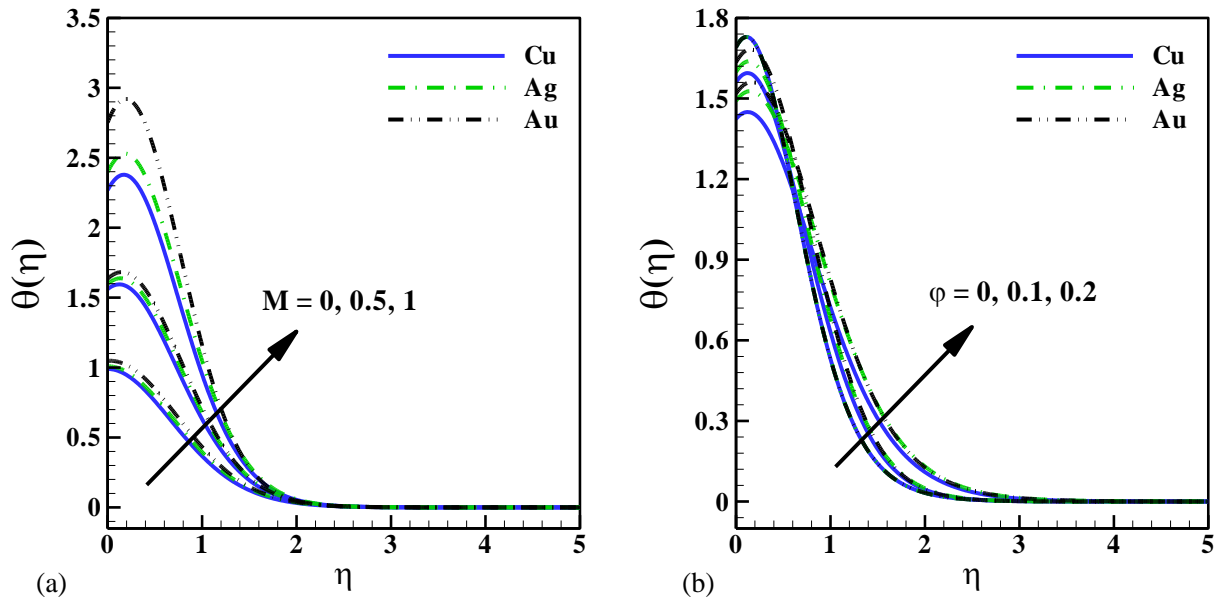
Fig. 4. Effects of magnetic parameter (M) and solid volume fraction (φ) on temperature.
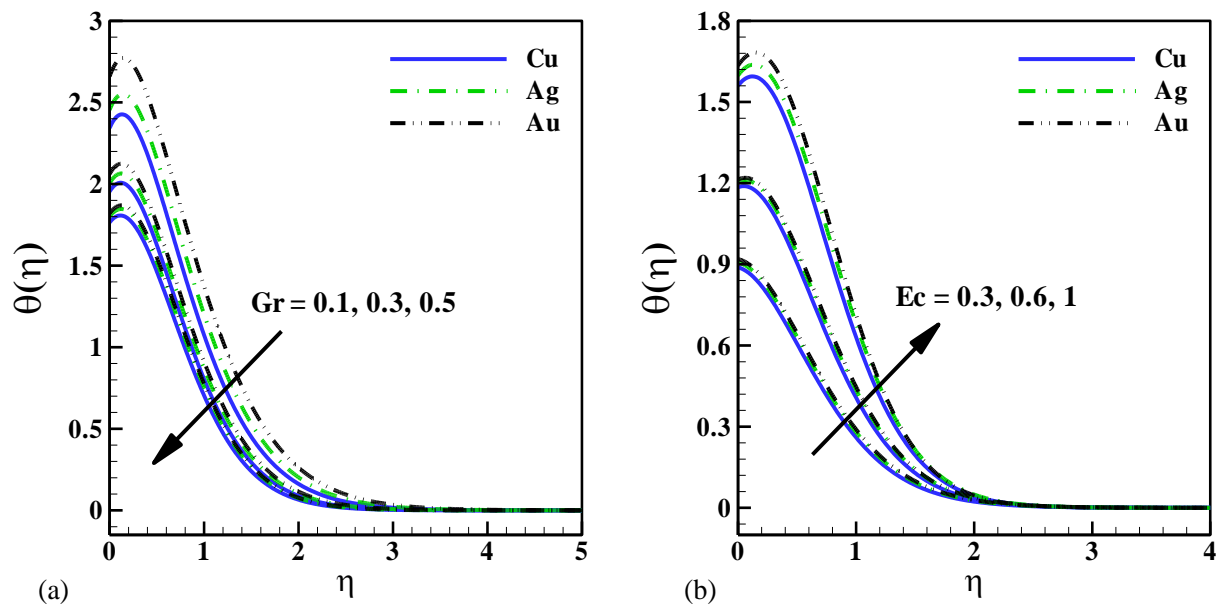
Fig. 5. Effects of thermal Grashof number (Gr) and Eckert number (Ec) on temperature.
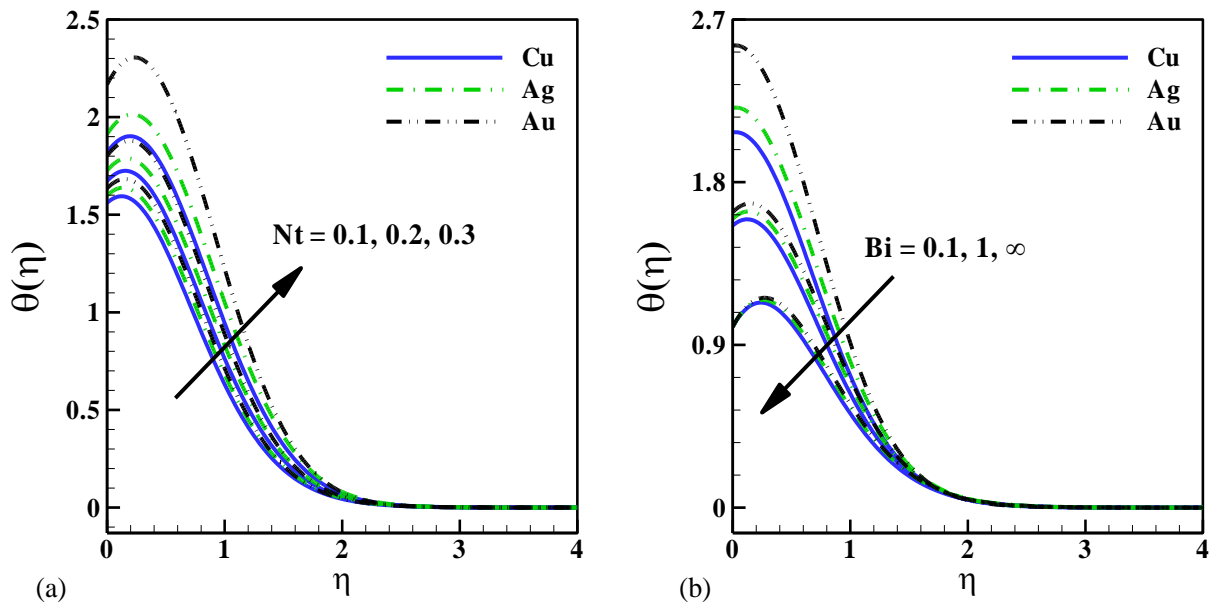
Fig. 6. Effects of Thermophoresis parameter (Nt) and Biot number (Bi) on temperature.
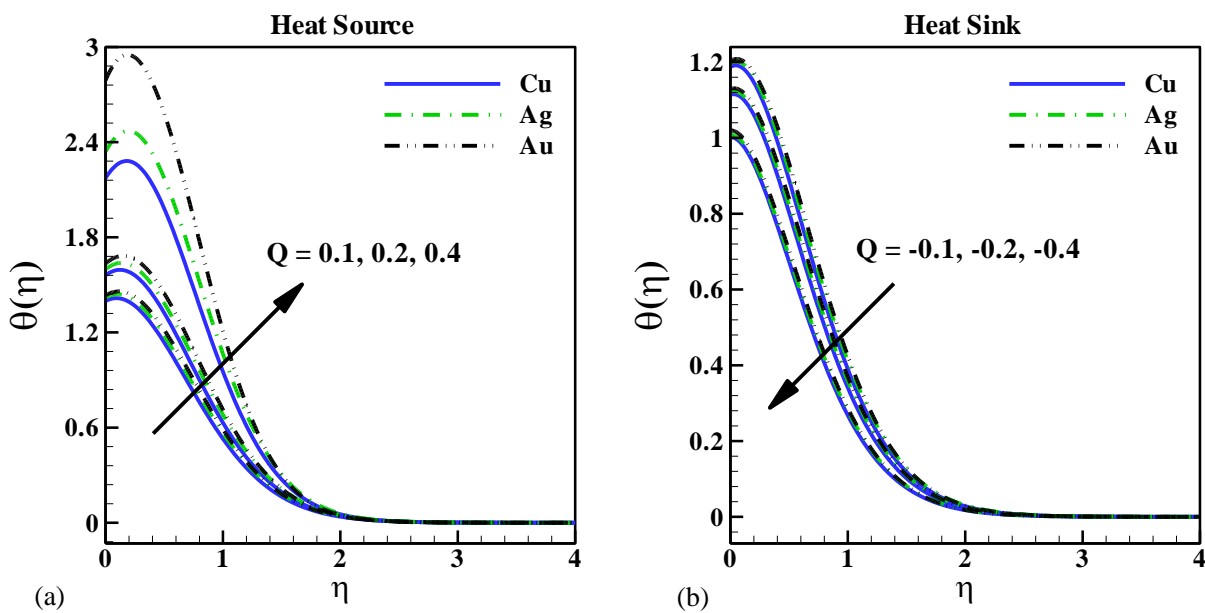
Fig. 7. Effects of Heat source/Sink parameter (Q) on temperature.
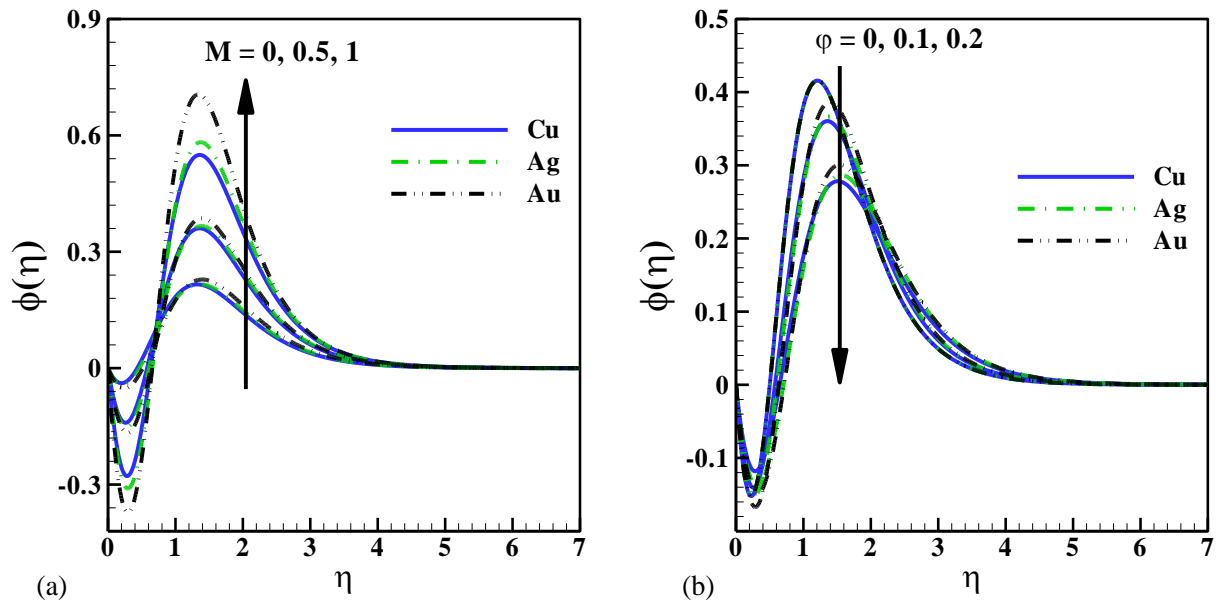
Fig. 8. Effects of magnetic parameter (M) and solid volume fraction (φ) on concentration.
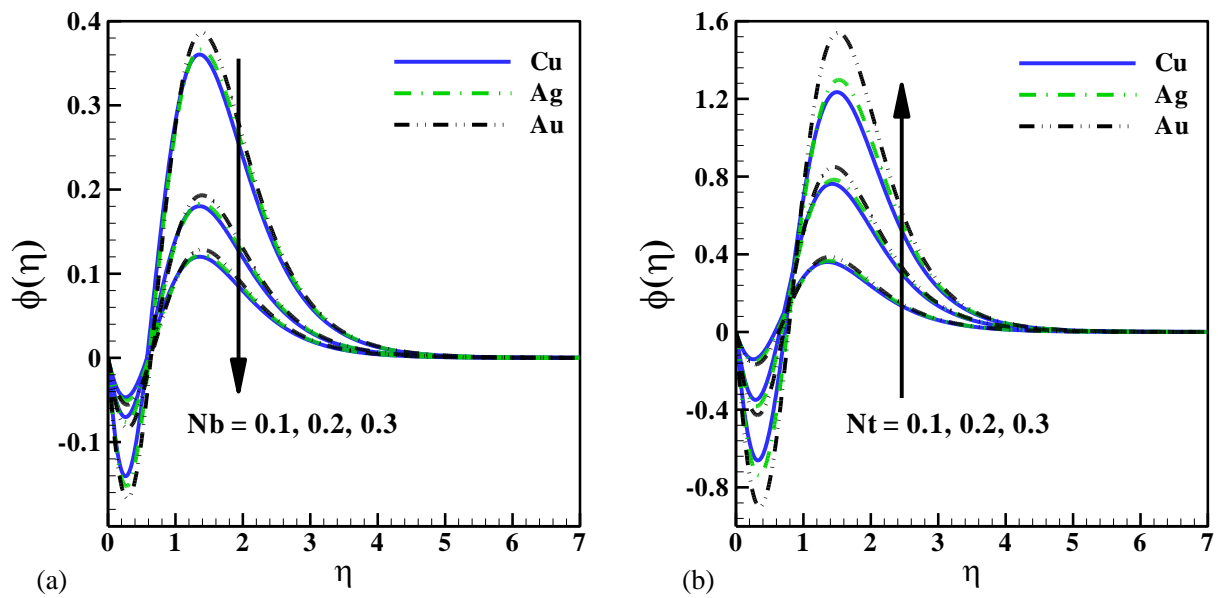
Fig. 9. Effects of Brownian motion parameter (Nb) and Thermophoresis parameter (Nt) on concentration.
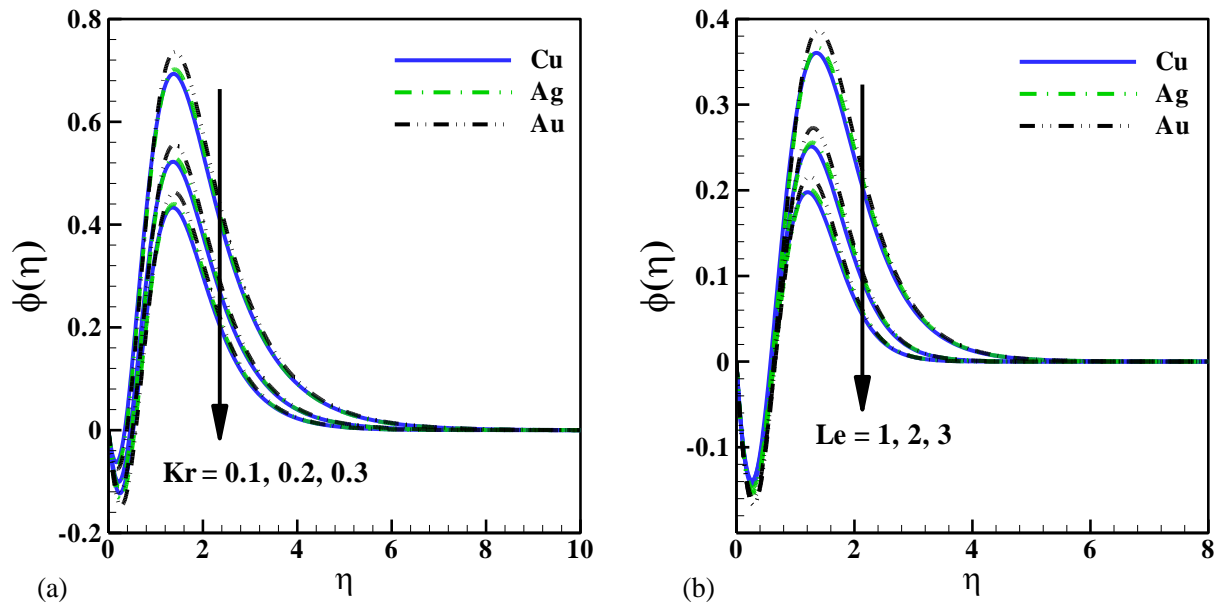
Fig. 10. Effects of Chemical reaction parameter (Kr) and Lewis number (Le) on concentration.
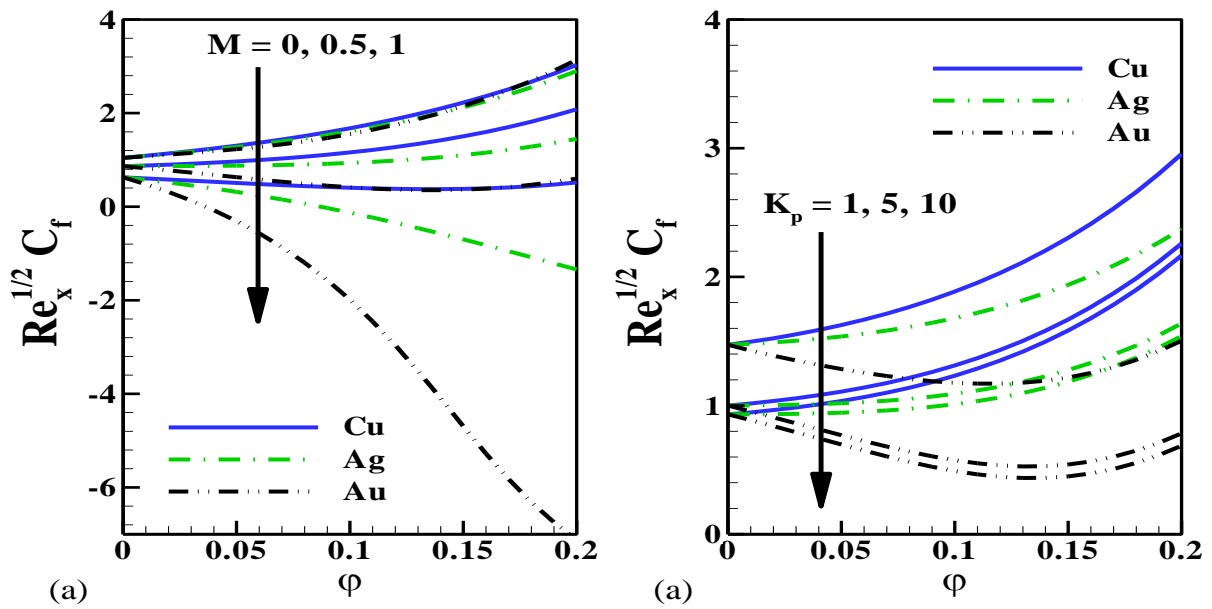
Fig. 11. Effects of magnetic parameter (M) and permeability parameter (K_p) on Skin friction.
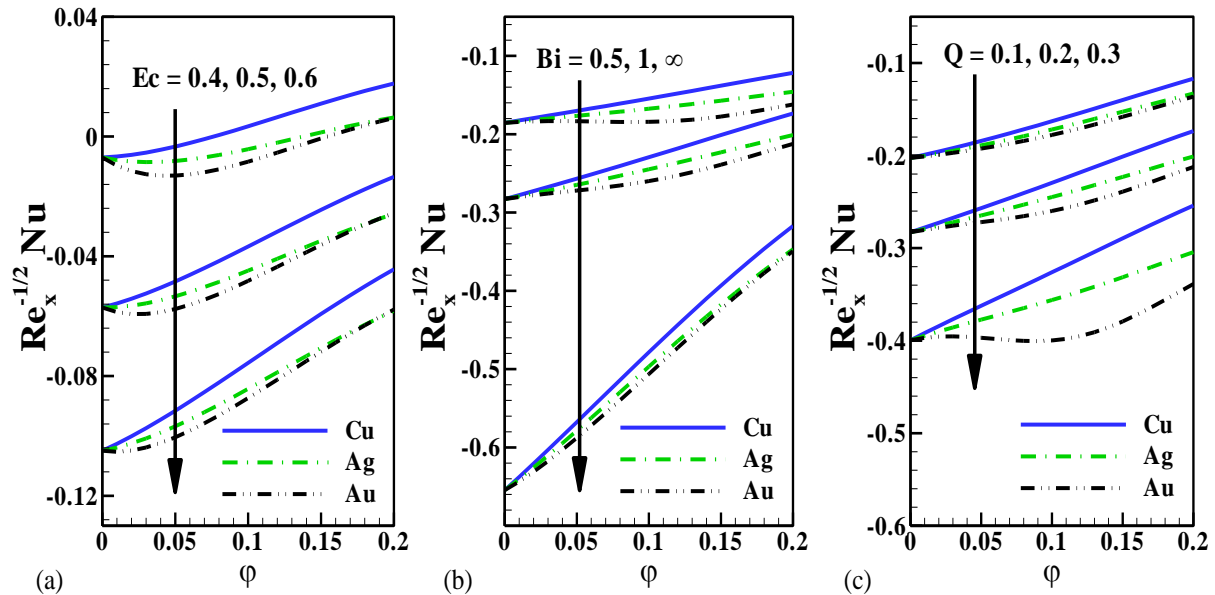
Fig. 12. Effects of Eckert number (Ec), Biot number (Bi) and heat source/sink parameter (Q) on Nusselt number.
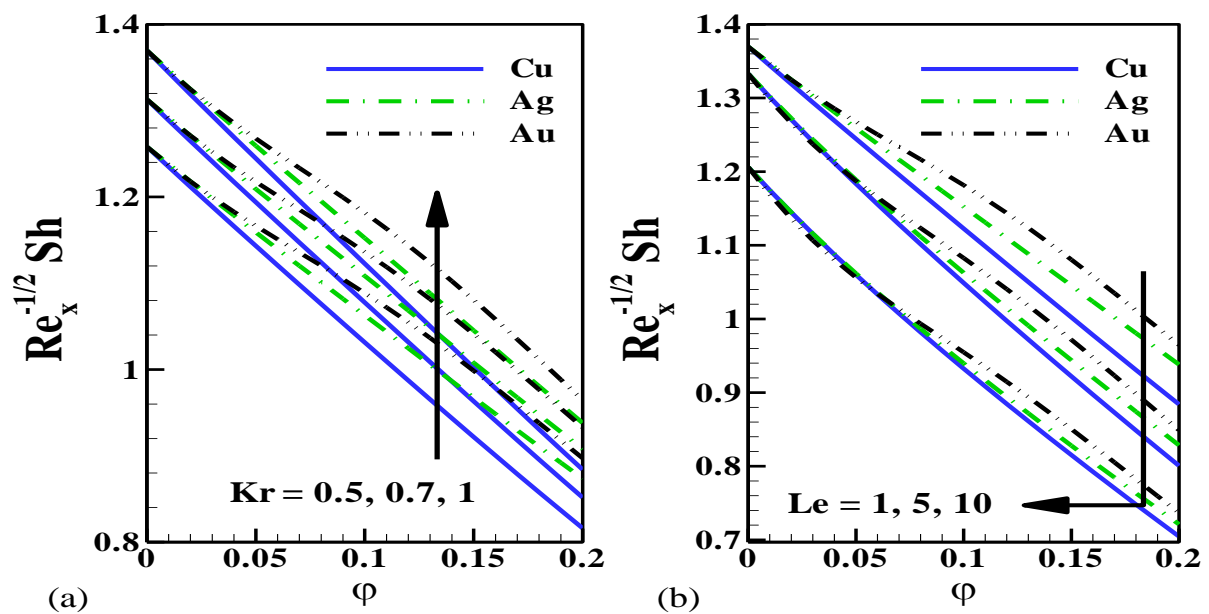
Fig. 13. Effects of chemical reaction parameter (Kr) and Lewis number (Le) on Sherwood number.

4.1. Velocity profiles

Fig 2 shows the evolution in $f'(\eta)$ profiles for different nanoparticles for variations in M and φ. **Fig 2a** indicates that the flow velocity is high near the wall for all the nanoparticles; however, with increment in M and *progressively higher magnetic field*, velocity is suppressed, and momentum boundary layer thickness is increased. As expected, velocity profile clearly decreases as M increases and this is linked with the resistive nature of the body Lorentz force which inhibits momentum development. The *classical velocity overshoot* is

observed to be very prominent for maximum magnetic field effect ($M = 1$) for gold nanoparticles, a weaker overshoot is observed for silver nanoparticles and there is an absence in velocity overshoot for copper nanoparticles. *Ag* produces maximum velocity while *Cu* achieves the least velocity. Fig 2b shows the response in velocity $f'(\eta)$ with the transverse coordinate to a modification in nanoparticle volume fraction again for gold, silver and copper nanoparticles. It is evident that a strong depletion in the flow is generated with higher fractional volume of nanoparticles i. e. the thickness of the hydro-dynamic boundary layer reduces. Silver nanomaterial *Ag* produces maximum velocities while *Au* achieves the least.

Velocity plots for different thermal Grashof number (Gr) and porosity parameter (K_p) respectively are illustrated in **Fig 3**. The thermal buoyancy parameter (Gr) significantly boosts the velocity distribution by mobilizing more intense thermal convection currents near the wall as depicted in Fig 3a. When $Gr = 0$, thermal buoyancy is negated and *forced convection* arises. As the buoyancy effect is enlarge the thermal convective influence on the nanoparticles is magnified. Intensification of free convection currents in the energy boundary layer encourages migration of nanoparticles away from the hot wall. The thermal buoyancy force in the velocity Eqn. (9) i. e. $A_1, A_2, A_3, Gr\theta$, couples *this equation to the energy* Eqn. (10). Hence, the thermofluid characteristics are strongly influenced by Grashof number and there is an intimate interplay between viscous force and thermal buoyancy force. Laminar flow is however sustained since turbulence requires exceedingly higher Grashof numbers. Fig **3b** presents the evolution of nanofluid flow characteristics on $Cu - Ag - Au$ nanoparticles with the porous medium permeability parameter (K_p). Velocity profile topologies reveal that initially although there is a strong acceleration (owing to the sparsity of packing of solid fibers near the wall), gradually the *dominant effect* is to decelerate the flow with higher values of K_p. The linear Darcian bulk porous matrix impedance is simulated via the term, $-(1/K_p)f'$ in the momentum Eqn. (9). Although this term is significantly of lower order than the shear terms in the same equation, it has a profound effect on hydrodynamics. As K_p increases, the porosity is enhanced, and greater inter-pore space is made available for the percolating nanofluid. The resistance is therefore simultaneously reduced, and the flow is markedly slow down. This inhibiting effect have been confirmed in numerous other studies of nanofluid transport in porous media - see [32-35]. Although geometric characteristics of the porous matrix structure cannot be simulated with the Darcy model, which is defensible for viscous-dominated flows (up to Reynolds numbers of approximately 10), it provides a much easier methodology for incorporating porous drag outcome in the framework of boundary layer flow models. Of course, in the limit of infinite permeability (hydraulic conductivity), $K_p \to \infty$, solid fibers vanish in the medium and the purely nanofluid case is retrieved. Overall, the inclusion of a porous medium offers a *simple but impactful mechanism for regulating the flow structure and also associated heat transfer* in the materials processing regime. It is further noteworthy that the present study is confined to *isotropic, homogenous media*. Anisotropic effects [36-38] and also non-Darcy inertial drag effects (Forchheimer impedance) [39-42] may also arise and these may be considered in future studies.

4.2. Temperature profiles

Fig 4 demonstrates the impact of (M) and (φ) on the temperature plots. The additional work utilized in dragging the nanofluid in opposition to the action of a magnetic field, is dissipated as thermal energy. This heats the boundary layer regime and enhances thermal boundary layer thickness. Temperatures are therefore *minimized* in the absence of magnetic field $(M = 0)$ i. e. the *electrically non-conducting* nanofluid case. Since Joule heating is also present in the term, $A_4 M\ Ec\left(f'\right)^2$, the magnetic effect is also directly encountered in the heat transfer Eqn. (10). Therefore, while significant damping is induced in the velocity field, the thermal distribution experiences a different effect. (Fig 4a). The *gold nanomaterial* produces maximum temperatures while *copper achieves the least temperatures*. It is apparent from Fig 4b that a strong accentuation in temperature is mobilized with higher nanoparticle volume fractions i. e. greater doping percentage of the base fluid. The flow distributions indeed confirm the non-trivial effect of nanoparticle doping as a strong mechanism for elevating both convection and conduction coefficients. Hence, nanofluids are effective for energizing base fluids without the clogging effects encountered with micro-scaled particles. They increase thermal efficiency of processes and these are beneficial in coating dynamics since an *extra mechanism* is available for regulating heat transfer effects and more precisely manipulating finishing characteristics. The gold nanoparticles, *Au* produce maximum temperatures while *copper produces the lowest temperatures i. e. strongest cooling within the bulk nanofluid*.

The physical impact of thermal buoyancy on evolution of nanofluid temperature is displayed in **Fig 5(a)**. $Gr > 0$ corresponds to natural (free) convection in which intensified thermal convection currents produce cooling of the sheet (plate) i. e. a depletion in temperatures near the plate with a point of inflection computed in the vicinity of $\eta < 3$. Beyond this point however a heating effect is observed i. e. thermal boundary layer is thickened. In Fig. 5b, it is clearly observed that the higher value of viscous heating parameter, Eckert number, Ec, *produces a thicker thermal boundary layer and higher temperature*, irrespective of the nanoparticle considered. There is *an accentuation in conversion of kinetic energy in the boundary layer flow to thermal energy* owing to internal friction with higher Eckert numbers. In both figs. 5a, b, the classical temperature overshoots near the plate surface are captured accurately and are most prominent for gold nanoparticles and diminished for copper nanoparticles, with silver falling in between these two extremities. Asymptotically smooth solutions are achieved in the free stream (edge of the boundary layer i. e. at η_{max}) authenticate the authorization of a competently substantial infinity boundary condition in the MATLAB quadrature code.

From **Fig 6(a)**, it is evident that a stronger temperature field is generated via an increment in values of thermophoresis parameter (Nt). Strong accentuation in the temperature is influenced with an increase in Nt and this is due to mobilization of heat diffusion under temperature gradient through nanoparticle micro-convection, as noted in [43]. **Fig 6(b)** illustrates the effect of Biot number on the nanofluid temperature. The Biot number implies the potency of convective heating. The ratio of internal conductive to the surface convective is expressed via the Biot number. In the case of $Bi = 0$, an *isoflux wall situation* is observed since the heat flux at the boundary is fixed whereas for the *isothermal wall case* as $Bi \to \infty$ leads to the temperature at the boundary being fixed. Temperatures clearly diminish with greater Biot number. The gold nanoparticles

achieve consistently the highest temperatures (thicker thermal boundary layer) while copper corresponds to the lowest temperatures (thinner thermal boundary layer). Once again very smooth distributions (decays) are computed in the free stream, confirming the prescription of a sufficiently large infinity boundary condition in the MATLAB quadrature solution.

Fig 7a depicts the temperature distribution for the effects of heat source $(Q > 0)$ and heat sink $(Q < 0)$ parameters. In certain thermal coating operations, either heat generation (hot spot) or a cooling spot (heat sink) can be employed to manipulate heat build-up in the boundary layer. Fig 7 (a) indicates a strong boost in temperatures with elevation in the heat source term; this exacerbates the heat diffusion in the regime and thickens the thermal boundary layer on the vertical surface. The reverse trend is computed with increasing heat sink as shown in Fig 7 (b). Once again gold nanoparticles correspond to peak temperatures, then silver and finally copper nanoparticles.

4.3. Nanoparticle concentration profiles

Figs. 8(a) and (b) visualize the nanoparticle concentration distributions for the effects of magnetic field (M) and solid volume fraction parameter (φ). Increasing M enhances the nanoparticle species concentration magnitudes considerably whereas the opposite trend is induced with increment in volume fraction parameter. Although absent in the nanoparticle species conservation Eqn. (11), magnetic field directly influences temperature and velocity fields. The coupling terms i.e. $(Nt / Nb)\theta''$ and $f\phi'$ in the nanoparticle species Eqn. (11) connect the concentration field to the energy (10) and momentum (9) equations. Therefore, species diffusion characteristics are indirectly modified with stronger magnetic field *and nanoparticle diffusion is assisted*.

Fig 9(a) and (b) respectively illustrate the nanoparticle concentration distribution for the effects of Brownian motion and thermophoresis parameter. Increasing Nb diminishes the solutal profile whereas the impact is opposite for an increment in thermophoresis parameter. Smaller nanoparticle size corresponds to larger Nb value and this implies greater ballistic collisions which inhibits the diffusion of the nanoparticles and reduces both concentration and species boundary layer thickness.

Fig 10 a, b, present the evolution in nanoparticle concentration profiles for the influence values of *chemical reaction parameter, Kr and Lewis number, Le*. A substantial reduction in the nanoparticle concentration (Fig. 10a) is observed with stronger chemical reaction since a greater mass of nanoparticles is converted into another species. This depletes the nanoparticle concentration boundary layer thickness. However, there is an *undulating nature* to the response. Very close to the plate surface there is an initial plummet in concentrations irrespective of gold, silver or copper nanoparticles, and only thereafter do profiles ascend. A peak is attained some distance transverse to the plate surface and only then does a decay ensue which is sustained into the freestream. Fig 10(b) portrays the impact of Lewis number on nanoparticle species concentration profiles. Lewis number embodies the ratio of thermal diffusivity to mass (species) diffusivity. It also characterizes the relative thickness of thermal and species boundary layers. Larger Le values imply smaller molecular diffusivity and smaller values imply higher diffusivity. This is also related to the density of nanoparticles. It is apparent that *lower Lewis number* encourages nanoparticle diffusion and enhances concentration magnitudes, corresponding to lighter molecular weights of the diffusing species. The opposite effect is induced with *higher Lewis number*. Only for $Le = 1$ are both thermal and species diffusion rate

equivalent and both thermal and nanoparticle (species) concentration boundary layers have equal thickness in the flow regime.

4.4. Shear stress, heat transfer and mass transfer profiles

Fig 11 analyzes the response in velocity gradient i. e. dimensionless surface shear stress with an increment in M, K_p and φ. An attenuation in skin friction is produced with enhanced values of M, K_p and φ i. e stronger magnetic field, greater porous medium permeability and nanoparticle volume fraction all elevate skin friction at the plate surface.

       Fig 12 illustrates the impact of Ec, Bi, Q and φ on Nusselt number. The heat transfer rate decreases with increasing Ec, Bi, Q and φ i. e. although these parameters increase bulk nanofluid temperature, they reduce the rate of heat transmitted to the boundary and depress Nusselt numbers.

       Finally, **Fig 13** depicts the impact of Kr, Le and φ on Sherwood number. The boost in the wall mass transfer rate i. e. *gradient of nanoparticle concentration* is elevated with increasing chemical reaction parameter (since nanoparticle concentrations in the boundary layer are reduced) whereas the *contrary response* is observed with increasing Lewis number. In both plots the Sherwood number is suppressed with greater nanoparticle volume fraction. Again, *maximum* Sherwood numbers (as with Nusselt number and skin friction) correspond to the *gold nanoparticle case*, with the next highest magnitudes for the silver nanoparticle case and the lowest recorded for the copper nanoparticle case.

5. Conclusions

A theoretical and computational study of chemically reacting hydromagnetic nanofluid flow with thermophoretic diffusion, Brownian motion and Ohmic magnetic heating (Joule dissipation) in a Darcian permeable regime has been presented, as a model of multi-physical nanomaterials processing. The current flow model also considers a number of different nanofluid types- Cu (Copper), Ag (Silver) and Au (Gold) nanoparticles with base fluid $C_2H_60_2$ (Ethylene-Glycol). Effectively a nanoscale formulation (thermophoresis and Brownian motion) combining the Buongiorno two-component model with the Tiwari-Das model is deployed so that a nanoparticle species diffusion equation is also included as well as material properties for specific nanoparticles and base fluids. The major results of the computations may be outlined as follows:

- Generally gold Au nanoparticles (black dashed lines in the graphs) achieve the highest magnitudes in all quantities (velocity, temperature and nano-particle concentration), irrespective of the parameter being varied, the next highest values are obtained with silver Ag nanoparticles (green dashed lines) and the lowest values with copper Cu nanoparticles (blue solid lines).

- A *velocity overshoot* is computed for maximum magnetic field effect ($M = 1$) for gold nanoparticles, a weaker overshoot for silver nanoparticles and there is an absence in velocity overshoot for copper nanoparticles.

- An enhancement in M, Gr, K_p accelerates boundary layer flow (thinner momentum boundary layer) whereas elevation in nanoparticle volume fraction, φ induces a deceleration (thicker momentum boundary layer).

- Temperatures are suppressed with greater Gr, Bi, whereas they are boosted with higher values of M, φ, Ec, Nt and Q. Both magnetic field and Ohmic magnetic dissipation exert a substantial effect on temperature distributions by inducing significant heating.

- Substantial elevation in nanoparticle concentrations is generated with increment in thermophoresis parameter whereas as a depletion is generated with an increase in Brownian motion parameter; furthermore, increasing Lewis number (related to lower molecular diffusivity of nanoparticle species) also enhances nano-particle concentration throughout the boundary layer domain.

- An increase in M and K_p, i. e. stronger transverse magnetic field and increasing porous medium permeability respectively reduces and enhances the skin friction.

- An increase in Ec, Bi, Q suppresses Nusselt number, whereas increasing Lewis number (lower species diffusivity) favourably influences Sherwood number.

- Finally, thermophoresis and Brownian motion are found to be significant effects in improving heat transportation phenomena in all nanofluids.

The present computations have been restricted to magnetic field effects. Electrical fields and electrokinetic phenomena have been ignored and can be analyzed to generalize the current model to electro-magneto-nanofluid transport [43]. Furthermore, interesting extensions to the current work may also address turbulence [44], micro-organism doping and wall slip [45], nano-particle shape effects [46] and non-Newtonian behaviour for gold-water nanofluids [47]. These aspects are currently under investigation.

Acknowledgments

References

[1] Choi, S. U. S. Eastman JA. Enhancing thermal conductivity of fluids with nanoparticles. *Materials Science* 231, 99–105 (1995).

[2] Ogunseye, H.A., Salawu, S.O., Tijani, Y.O., Riliwan, M. and Sibanda, P. Dynamical analysis of hydromagnetic Brownian and thermophoresis effects of squeezing Eyring-Powell nanofluid flow with variable thermal conductivity and chemical reaction. *Multidiscipline Modeling in Materials and Structures* 15(6), 1100-1120 (2019).

[3] Makinde, O.D. and Mishra, S.R. On stagnation point flow of variable viscosity nanofluids past a stretching surface with radiative heat. *International Journal of Applied and Computational Mathematics* 3(2), 561-578 (2017).

[4] Ramesh, G.K., Chamkha, A.J. and Gireesha, B.J. Magnetohydrodynamic flow of a non-Newtonian nanofluid over an impermeable surface with heat generation/absorption. *Journal of Nanofluids* 3, 78–84 (2014).

[5]   V. Rajesh, M.P. Mallesh and O. Anwar Bég, Transient MHD free convection flow and heat transfer of nanofluid past an impulsively started vertical porous plate in the presence of viscous dissipation, *Procedia Materials Science,* 10, 80-89 (2015).

[6]   V.R. Prasad, S. A. Gaffar and O. Anwar Bég, Non-similar computational solutions for free convection boundary-layer flow of a nanofluid from an isothermal sphere in a non-Darcy porous medium, *J. Nanofluids*, 4, 1–11 (2015).

[7]   M.J. Uddin, O. Anwar Bég and N.S. Amin, Hydromagnetic transport phenomena from a stretching or shrinking nonlinear nanomaterial sheet with Navier slip and convective heating: a model for bio-nano-materials processing, *J. Magnetism Magnetic Materials,* 368, 252-261(2014).

[8]   O. Anwar Bég, M. Ferdows, S. Islam and M. Nazrul Islam, Numerical simulation of Marangoni magnetohydrodynamic bio-nanofluid convection from a non-isothermal surface with magnetic induction effects: a bio-nanomaterial manufacturing transport model, *J. Mechanics Medicine Biology*, 14, 1450039.1-1450039.32 (2014).

[9]   Rarani, E.M., Etesami, N. and Nasr, E.M. Influence of the uniform electric field on viscosity of magnetic nanofluid (Fe3O4-EG). *Journal of Applied Physics* 112(9), 094903 (2012). https://doi.org/10.1063/1.4763469

[10]   Kandasamy, R., Loganathan, P. and Arasu, P.P. Scaling group transformation for MHD boundary-layer flow of a nanofluid past a vertical stretching surface in the presence of suction/injection. *Nuclear Engineering Design* 241(6), 2053-2059 (2011).

[11]   Anwar Bég, O., Kuharat, S., Ferdows, M., Das, M., Kadir, A. and Shamshuddin, MD. Modelling magnetic nanopolymer flow with magnetic induction and nanoparticle solid volume fraction effects: solar magnetic nano-polymer fabrication simulation. *Proceedings of IMechE-Part N: Journal of Nanoengineering Nanomaterial and Nanosystems 233*(1), 27-45 (2019).

[12]   Makinde, O.D. and Animasaun, I.L. Thermophoresis and Brownian motion effects on MHD bioconvection of nanofluid with nonlinear thermal radiation and quartic chemical reaction past an upper horizontal surface of a paraboloid of revolution. *Journal of Molecular Liquids* 221, 733-743 (2016).

[13]   Mondal, M., Biswas, R., Shanchia, K., Hasan, M., Ahmmed, S.F. Numerical investigation with stability convergence analysis of chemically hydromagnetic Casson nanofluid flow in the effects of thermophoresis and Brownian motion. *International Journal of Heat and Technology 37*(1), 59-70 (2019).

[14]   Pakravan, H.A. and Yaghoubi, M. Combined thermophoresis, Brownian motion and Dufour effects on natural convection of nanofluids. *International Journal of Thermal Sciences* 50(3), 394-402 (2011).

[15]   Kuznetsov, A.V. and Nield, D.A. Natural convective boundary layer flow of a nanofluid past a vertical plate: A revised model. *International Journal of Thermal Sciences* 77, 126-129 (2014).

[16]   Aminfar, H. and Haghgoo, M.R. Brownian motion and thermophoresis effects on natural convection of alumina-water nanofluid. *Proceedings of IMchE-Part C: Journal of Mechanical Engineering and Sciences* 227(1), 100-110 (2012).

[17]   Shamshuddin, MD. And Eid, M.R. nth order reactive nanoliquid through convective elongated sheet under mixed convection flow with joule heating effects. *Journal of Thermal Analysis and Calorimetry* (2021). https://doi.org/10.1007/s10973-021-10816-0.

[18] Zhang, C., Zheng, L., Zhang, X. and Chen, G. MHD flow and radiation heat transfer of nanofluids in porous media with variable heat flux and chemical reactions. *Applied Mathematics and Modeling* 39(1), 165-181 (2015).

[19] Qayyum, S., Khan, M.I., Hayat, T. and Alsaedi, A. A framework for nonlinear thermal radiation and homogenous-heterogenous reactions flow based on silver-water and Copper-water nanoparticles: A numerical model for probable error. *Results in Physics* 7, 1907-1914 (2017).

[20] Salawu, S.O., Kareem, R.A., Shamshuddin, MD. and Khan, S.U. Double exothermic reaction of viscous dissipative Oldroyd-8 constant fluid and thermal ignition in a channel. *Chemical Physics Letters* 760, 100732 (2020). https://doi.org/10.1016/j.cplett.2020.138011.

[21] Mishra, S.R., Shamshuddin, MD., Anwar Bég, O. and Kadir, A. Adomain computation of radiative-convective bi-directional stretching flow of a magnetic non-Newtonian fluid in porous media with homogenous-heterogenous reactions. *International Journal of Modern Physics. B* 34(18), 2050165 (2020). https://doi.org/10.1142/S021797922001659

[22] Aleem, M., Asjad, M.I., Shaheen, A. and Khan, I. MHD influence on different water based nanofluids (TiO$_2$, Al$_2$O$_3$, CuO) in porous medium with chemical reaction and Newtonian heating. *Chaos, Solitons & Fractals* 130, 109437 (2020). https://doi.org/10.1016/j.choas.2019.109437

[23] Ullah, I., Shafie, S., Makinde, O.D. and Khan, I. Unsteady MHD Falkner-Skan flow of Casson nanofluid with generative/destructive chemical reaction. *Chemical Engineering Science* 173, 694-706 (2017).

[24] Haile, E. and Shankar, B. Heat and mass transfer through a porous media of MHD flow of nanofluids with thermal radiation, viscous dissipation and chemical reaction effects. *American Chemical Science Journal* 4(6), 828-846 (2014).

[25] Mishra, A.K., Pattnaik, P.K., Mishra, S.R. and Senapati, N. Dissipative heat energy on Cu and Al$_2$O$_3$ ethylene-glycol-based nanofluid flow over a heated semi-infinite vertical plate. *Journal of Thermal Analysis and Calorimetry* (2020). https://doi.org/10.1007/s10973-020-09666-z

[26] Sheikholeslami, M. and Ganji, D.D. Ferrohydrodynamic and magnetohydrodynamic effects on ferrofluid flow and convective heat transfer. *Energy* 75, 400-410 (2014).

[27] Wakif, A., Boulahia, Z. and Mishra, S.R. Influence of a uniform transverse magnetic field on the thermo-hydrodynamic stability in water-based nanofluids with metallic nanoparticle using the generalized Buongiorno's mathematical model. *European Physical Journal Plus* 133, 181 (2018). https://doi.org/10.1140/epjp/i2018-12037-7

[28] Mabood, F. and Das, K. Melting heat transfer on hydromagnetic flow of a nanofluid over a stretching sheet with radiation and second-order slip. *European Physical Journal Plus* 131, 3 (2016). https://doi.org/10.1140/epjp/i2016-16003-1

[29] Xu, L. and Lee, E.M.W. Variational iteration method for the magnetohydrodynamic flow over a nonlinear stretching sheet. *Abstract and Applied Analysis* 2013, 573782 (2013). https://doi.org/10.1155/2013/573782.

[30] Khan, W.A. and Pop, I. Boundary-layer flow of a nanofluid past a stretching sheet. *International Journal of Heat and Mass Transfer* 53, 2477–2483 (2010).

[31] Mabood, F., Ibrahim, S.M. and Khan, W.A. Framing the features of Brownian motion and thermophoresis on radiative nanofluid flow past a rotating stretching sheet with magnetohydrodynamics. *Results in Physics* 6, 1015–1023 (2016).

[32] Anwar Bég, O., Khan, M.S., Karim, I., Alam, M.M. and Ferdows, M. Explicit numerical study of unsteady hydromagnetic mixed convective nanofluid flow from an exponentially stretching sheet in porous media. *Applied Nanoscience* 4(8), 943-957 (2014).

[33] Anwar Bég, O., Prasad, V.R. and Vasu, B. Numerical study of mixed bioconvection in porous media saturated with nanofluid and containing oxytactic micro-organisms. *Journal of Mechanics in Medicine Biology* 13, 1350067.1-1350067.25 (2013).

[34] Uddin, M.J., Anwar Bég, O. and Ismail, A.I.M. Mathematical modelling of radiative hydromagnetic thermo-solutal nanofluid convection slip flow in saturated porous media. *Mathematical Problems in Engineering* 2014, 179172 (2014). https;//doi.org/10.1155/2014/179172.

[35] Anwar Bég, O., Motsa, S.S., Kadir, A., Bég, T.A. and Islam, M.N. Spectral quasilinear numerical simulation of micropolar convective wall plumes in high permeability porous media. *Journal of Engineering Thermophysics* 25(4), 1–24 (2016).

[36] Anwar Bég, O., Prasad, V.R., Vasu, B. and Gorla, R.S.R. Computational modelling of Magnetohydro-dynamic convection from a rotating cone in orthotropic Darcian porous media. *Journal of Brazilian Society of Mechanical Science and Engineering* 39, 2035–2054 (2017).

[37] Anwar Bég, O., Uddin, M.J., Bég, T.A., Kadir, A., Shamshuddin, MD. and Babaie, M. Modelling mass transfer from a rotating cone in anisotropic porous media with Stefan blowing and Navier slip. *Indian Journal of Physics* 94(6), 863-877 (2020).

[38] Norouzi, M., Dorrani, S., Shokri, H. and Anwar Bég, O. Linear stability analysis and CFD simulation of thermal "viscous fingering" instability in anisotropic porous media. *ASCE Journal of Engineering Mechanics* 147(4), 04021006.1-04021006-20 (2021).

[39] Anwar Bég, O., Zueco, J., Bég, T.A., Takhar, H.S. and Kahya, E. NSM analysis of time-dependent nonlinear buoyancy-driven double-diffusive radiative convection flow in non-Darcy geological porous media. *Acta Mechanics* 202, 181-204 (2009).

[40] Prasad, V.R., Vasu, B., Prashad, R. and Anwar Bég, O. Thermal radiation effects on magneto-hydrodynamic heat and mass transfer from a horizontal cylinder in a variable porosity regime. *Journal of Porous Media* 15(3), 261-281 (2012).

[41] Umavathi, J.C. and Anwar Bég, O. Numerical study of double-diffusive dissipative reactive convective flow in an open vertical duct containing a non-Darcy porous medium with Robin boundary conditions. *Journal of Engineering Mathematics* 119, 135-147 (2019).

[42] Umavathi, J.C. and Anwar Bég, O. Convective flow and heat transfer in a vertical rectangular duct containing a horizontal porous and fluid layer. *International Journal of Numerical Methods for Heat and Fluid Flow* 31(4), 1320-1344 (2020).

[43] Prakash, J., Siva, E.P., Tripathi, D. and Anwar Bég, O. Thermal slip and radiative heat transfer effects on electro-osmotic magneto-nanoliquid peristaltic propulsion through a microchannel. *Heat Transfer* 48(7), 2882-2908 (2019).

[44] Akbarzadeh M, Rashidi, S, Karimi, N and Ellahi R. Convection of heat and thermodynamic irreversibilities in two-phase, turbulent nanofluid flows in solar heaters by corrugated absorber plates. *Advanced Powder Technology* 29(9), 2243-2254 (2018).

[45] Waqas, H, Imran M, Muhammad, T, Sait, S. M. and Ellahi, R. On bio-convection thermal radiation in Darcy-Forchheimer flow of nanofluid with gyrotactic motile microorganism under Wu's slip over stretching cylinder/plate, *International Journal of Numerical Methods for Heat and Fluid Flow* 31(5), 1520-1546 (2021).

[46] Tripathi, D, Prakash, J, Tiwari, A. K. and Ellahi, R. Thermal, microrotation, electromagnetic field and nanoparticle shape effect on Cu-Cuo/blood flow in microvascular vessels, *Microvascular Research* 132, 104065 (2020). https://doi.org/10.1016/j.mvr.2020.104065

[47] Hussain, F, Ellahi, R, Zeeshan, A. and Vafai, K. Modelling study on heated couple stress fluid peristaltically conveying gold nanoparticles through coaxial tubes: A remedy for gland tumors and arthritis, *Journal of Molecular Liquids* 268, 149-155 (2018).

Nomenclature

a	Stretching rate [1/s]	Bi	Biot number
Ag	Silver nanoparticle	Au	Gold nanoparticle
A^*	Space parameter	B^*	internal heat source (sink)
B_0	Magnetic field strength	C	species concentration [kg/m^2]
C_w	Surface concentration	C_∞	ambient concentration
C_f	Dimensionless drag force	Cu	Copper nanoparticle
C_p	Specific heat [J/Kg K]	D_B	Brownian coefficient [m^2/s]
D_T	Thermophoresis coefficient [m^2/s]	Ec	Eckert number
h	Step size	h_f	Coefficient of heat transfer
J_w	Mass transport rate	k^*	Mean absorption coefficient
k_{nf}	Thermal conductivity [Wm^{-1}K^{-1}]	Kr	Chemical reaction parameter
Le	Lewis number	M	Magnetic parameter
N	Concentration buoyancy	n	Order of reaction
Nb	Brownian motion parameter	Nt	Thermophoresis parameter
Nu_x	Local Nusselt number	Pr	Prandtl number
q_r	Radiative heat flux [W/m^2]	q_w	heat transport rate
R	Thermal radiation parameter	Re$_x$	Local Reynolds number
T	Fluid temperature [K]	T_f	Convective temperature [K]
T_w	Temperature at the wall [K]	T_∞	Ambient temperature [K]

| u, v | Velocity components [m/s] | u_w | Plate velocity [m/s] |
| x | Distance along the surface [m] | y | Distance normal to surface [m] |

Greek symbols

τ	Heat capacity ratio	τ_w	shear stress
β_T	Volumetric thermal expansion	β_C	volumetric solutal expansion
ρ_f	Base fluid density [kg/m^3]	ρ_{nf}	density of nanoparticles [kg/m^3]
$\left(\rho c_p\right)_{nf}$	Heat capacity	μ_{nf}	Effective viscosity [kg m^{-1}s^{-1}]
σ^*	Stefan-Boltzmann constant	σ_{nf}	electrical conductivity [$\Omega^{-1}m^{-1}$]
ψ	Stream function [m^2/s]	η	similarity variable
λ	Mixed convection parameter	δ	optimal step size
$\in$	Tolerance error	θ	dimensionless temperature
φ	Dimensionless concentration	ϕ	solid volume fraction

Subscripts

w	quantities at wall
∞	quantities far away from surface
f	Base fluid
nf	Nanofluid